

Effect of Jet Length and Ambient Temperature on the Performance of a Two-Phase Jet Impingement Heat Sink Refrigeration System

Pablo A. de Oliveira, Jader R. Barbosa Jr.

*POLO Research Laboratories for Emerging Technologies in Cooling and Thermophysics,
Department of Mechanical Engineering, Federal University of Santa Catarina (UFSC),
Florianópolis, SC, 88040900, Brazil, Phone/Fax: (+ 55) 48 3721-7900*

Abstract

The jet impingement heat sink integrated with a compact oil-free R-134a vapor compression refrigeration system presented in a previous work [?] is now evaluated in terms of the influence of the compressor piston stroke, applied thermal load, orifice-to-heater distance (jet length) and ambient (hot end) temperature. The proposed heat sink is a compact active thermal solution for concentrated heat loads as it integrates the evaporator and the expansion device into a single unit, making use of a single two-phase impinging jet as the cooling mechanism. The present analysis is based on the coefficient of performance and other steady-state heat transfer parameters associated with the impinging jet (heat transfer coefficient and heater surface temperature). A reduction of the jet length promoted a more vigorous splattering of the jet on the heated surface, enhancing the droplet breakup, which in turn reduced significantly the critical heat flux. An increase of the hot reservoir temperature increased the jet impingement heat transfer

Email address: jrb@polo.ufsc.br (Jader R. Barbosa Jr.)

coefficient.

Keywords: Jet impingement, vapor compression, compact system, oil-free compressor, electronics cooling.

1. Introduction

The refrigerant may leave the test section (two-phase jet heat sink) with a significant liquid fraction, which is needed to maintain a high overall thermal conductance of the unit [?]. Therefore, an electrical trace heater wrapped around the compressor suction line was installed to guarantee a safe operation of the compressor. In a lab test device such as the present apparatus, Joule heating is easier to supply and control. However, in a real application, the superheating thermal energy may come from an internal heat exchanger (using the condenser as a heat source), not necessarily adding to the electrical supply to the system. The temperature of point 1 (compressor inlet in Fig. ??) was accurately controlled so as to maintain a fixed refrigerant superheating degree at the compressor inlet. The complete specification of setup components, measurement instrumentation and variable control strategies can be found in Refs. [? ?].

1.1. Two-Phase Jet Heat Sink

The novel heat sink combines the expansion device and the evaporator into a single cooling module using a two-phase impinging jet to remove the heat load from a small surface. The assembly of the two-phase jet heat sink in the experimental setup is presented in Fig. 1. The jet cooler is composed of a metallic cap, a polycarbonate jet impingement chamber, an internal orifice plenum, a polymeric unit that serves for thermal insulation and fluid drainage, a reservoir to collect the outlet two-phase mixture, a film heater and a copper block that emulates the electronic component.

This study explores two versions of the jet cooler, which differ in their

jet chamber heights. In both versions, the external dimensions are 80 mm (width) \times 80 mm (depth) and the heights are 112.5 mm and 93.5 mm for Figs. 1 (a) and (b), respectively. Fig. 1 (b) shows the [pressure and temperature](#) instruments to determine the thermodynamic state of the refrigerant at the inlet and outlet of the jet cooler and the RTDs used to estimate the heated surface temperature.

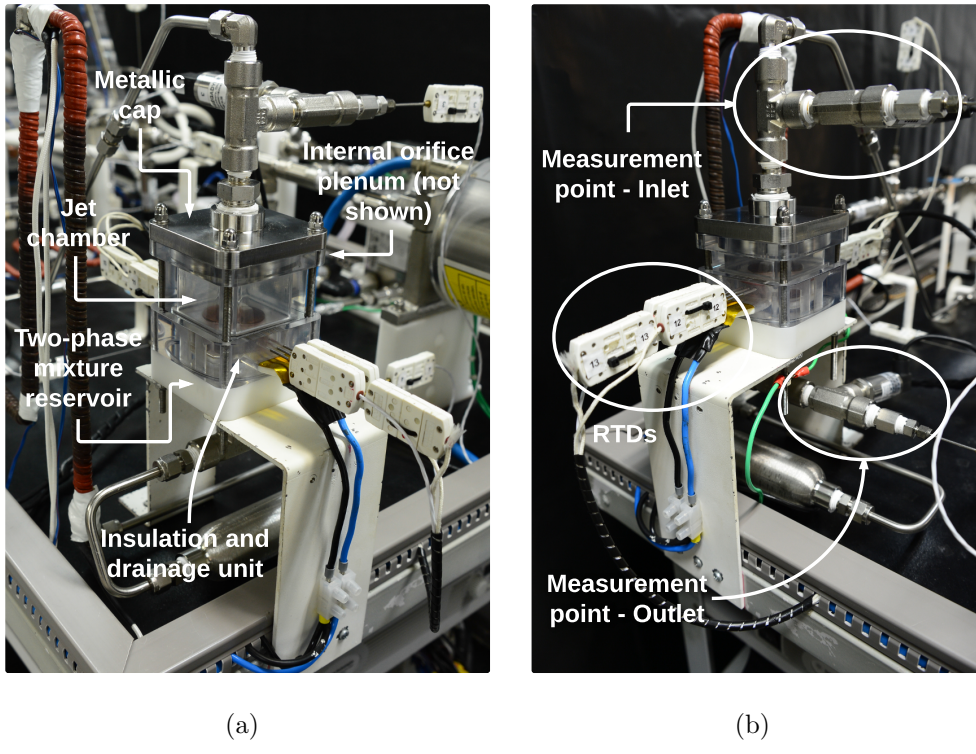


Figure 1: Two-phase jet coolers: assembly and main components. (a) 112.5-mm jet cooler, (b) 93.5-mm jet cooler

High-pressure sub-cooled liquid from the condenser flows through the metallic cap directly into the orifice plenum. The plenum, depicted in Fig. 2 (a), comprises an AISI 316 stainless steel outer orifice plate, a polyacetal resin

(POM) inner orifice plate and the expansion device, which is an array of POM 10-mm long threaded screws with the actual orifices drilled along their center lines – see Fig. 2 (b). The screws hold the orifice plates together. The plenum can accommodate up to 13 orifices in a staggered array covering a 20-mm side square area. In the present study, only single-jet tests are reported. In these tests, a $300\text{-}\mu\text{m}$ orifice screw was positioned at the center of the orifice plate assembly and dummy screws occupied the remaining positions, as shown in Fig. 3 (a).

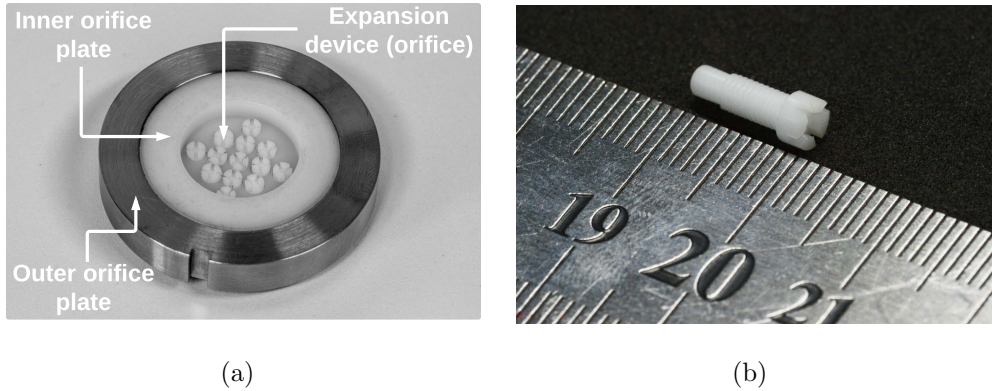


Figure 2: Orifice plenum: (a) assembled components and (b) expansion device ([threaded screw with an internal orifice](#)).

As the sub-cooled liquid passes through the nozzle it expands generating a downward-oriented jet inside the jet chamber. [The values of jet length, \$H\$, corresponding to the two jet chambers are](#) $H = 28.84$ and $H = 9.75$ mm, as shown in Fig. 3 (b). The jet length, i.e., the height of the chamber, is the vertical distance from the outlet of the orifice to the base of the chamber, which is at the same level of the impingement surface.

The impingement surface is the top surface of a heated cylindrical cop-

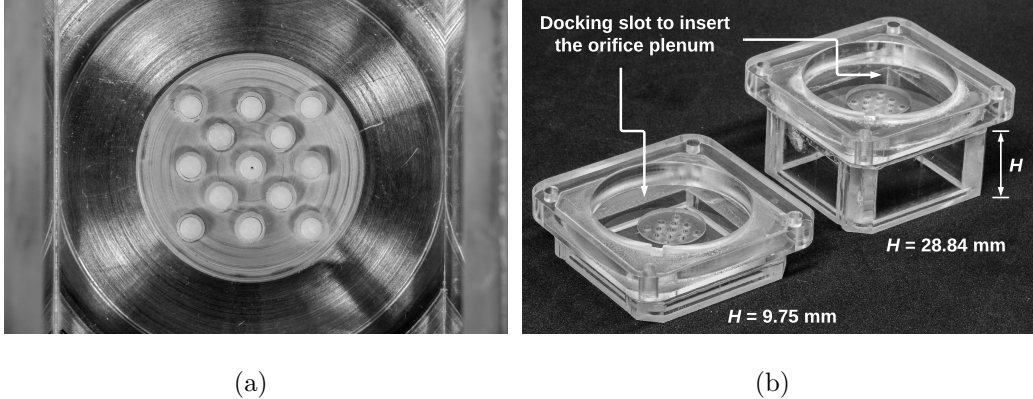


Figure 3: (a) Bottom view of the orifice plenum assembled in the jet chamber (300- μm orifice in the center). (b) Two jet chambers with different jet lengths.

per block mounted in a plastic bottom piece (insulation and drainage unit) designed to thermally insulate the sides and the bottom of the copper block and facilitate drainage of the two-phase mixture from the jet chamber into the reservoir. The heat source is a 200-W skin (thin film) heater [pressed tightly against \(and in good thermal contact with\) the bottom](#) of the copper block [by a teflon base plate, as seen in Fig. 4 \(a\)](#) [?]. The thermal load was finely controlled by a DC digital power supply. During the experimental runs, the thermal load was increased [in steps](#) by increasing the voltage or the current provided by the power supply. The copper block has six RTD wells, as shown in Fig. 4 (b). Five RTDs are used to measure the temperature and allow for an estimate of the surface temperature to be made using Fourier's law. The remaining one is connected to a commercial PID controller that functions as a safety system cutting the heating power supply in the event of a temperature runaway associated with the critical heat flux. The area of the target surface is 6.36 cm^2 ($D = 28.54 \text{ mm}$) and the distance from the

plane of the RTDs to the impingement surface is 10.03 mm.

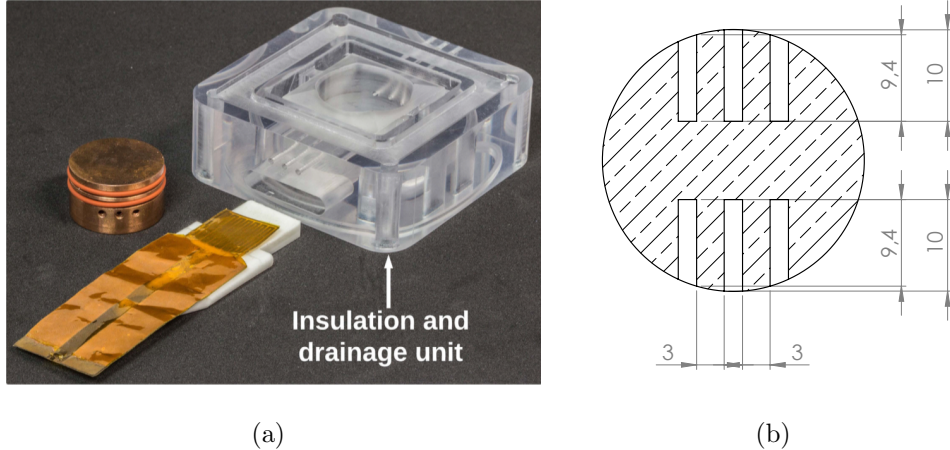


Figure 4: (a) Bottom side components of the jet cooler (copper block, teflon base plate, film heater, and insulation and drainage unit). (b) Cross-section view of the copper block at the RTDs' plane (dimensions in millimeters).

1.2. Experimental Conditions and Procedure

Experiments were conducted to investigate the influence of the following parameters on the system performance: (i) compressor piston displacement (stroke): 50%, 75% and 100% of the full stroke; (ii) applied thermal load (cooling capacity): 25 to 160 W (the maximum cooling capacity achieved in a particular test); (iii) jet length: 28.84 and 9.75 mm, and (iv) hot reservoir (ambient) temperature: 15°C and 25°C. A 300- μm orifice diameter size was used in all test runs. The mass flow rate of the WEG mixture was kept fixed at 180 kg/h. The room temperature and the calorimeter temperature were set at 25°C. The compressor inlet superheat, defined as $\Delta T_{sh} = T_1 - T_{evap}$, was kept fixed at 10°C (maximum expanded uncertainty of $\pm 0.31^\circ\text{C}$).

For a given piston stroke, α , the applied thermal load was increased in steps until the critical heat flux (CHF) was reached, which explains the different number of tests for each condition. The CHF was characterized experimentally by a sudden increase of the heater surface temperature and was confirmed by visual observations to coincide with a partial or total dryout of the liquid film on the heater surface.

The output (dependent) variables of the experimental apparatus are the refrigerant mass flow rate, pressures, temperatures, refrigerant sub-cooling degree at the outlet of the condenser, vapor mass quality at the outlet of the two-phase jet cooler, heat transfer rates and compressor power. Based on the output variables, the jet impingement heat transfer coefficient and the system coefficient of performance were calculated.

All output data were recorded during a 15-minute interval, after guaranteeing that the variation of each experimental variable between the beginning and the end of that interval was less than two times the standard deviation associated with the measurements of that variable. Another criterion satisfied by each variable prior to data recording was the variable standard deviation over the 15-minute interval to be lower than or equal to the corresponding overall experimental uncertainty.

1.3. Dependent Variables and Performance Metric

Energy balances between the inlet and outlet of the condenser and superheating line (see Fig. ??) can be written as:

$$\dot{Q}_{cond} = \dot{m}_r (h_3 - h_4) \quad (1)$$

$$\dot{Q}_{sh} = \dot{m}_r (h_1 - h_6) \quad (2)$$

where \dot{m}_r is the refrigerant mass flow rate and the refrigerant enthalpy at the compressor inlet, h_1 , condenser inlet, h_3 , and condenser outlet, h_4 , were computed via REFPROP 8.0 [?] using the local experimental values of pressure and temperature.

The refrigerant enthalpy at the outlet of the two-phase jet cooler, h_6 , was calculated from the energy balance on the cooler, neglecting the kinetic and potential energy contributions. Thus:

$$h_6 = h_5 + \frac{\dot{Q}_c}{\dot{m}_r} \quad (3)$$

where \dot{Q}_c is the cooling capacity and the refrigerant specific enthalpy at the inlet of the jet cooler, h_5 , was also determined from local measurements of pressure and temperature At steady state, the cooling capacity is equal to the thermal load imposed by the skin heater, considering a perfectly insulated test section.

The vapor mass quality at the exit of the jet cooler, x_6 , was determined from h_6 and the measured outlet pressure, P_6 . The saturation pressures were calculated directly from the experimental data, i.e., $P_{evap} = P_6$ and $P_{cond} = P_4$, both taken at the outlets of the jet cooler and condenser, respectively.

The indicated power, i.e., the useful work performed on the refrigerant by the piston per unit time, can be determined by the following equation,

$$\dot{W}_{ind} = \dot{m}_r (h_2 - h_1) \quad (4)$$

where h_2 is the enthalpy at the compressor outlet computed using the local experimental values of pressure and temperature.

The jet impingement heat transfer coefficient, \hbar , is a key parameter in the design of the two-phase jet cooler. It is defined by:

$$\hbar = \frac{\dot{Q}_c^*}{A_s(T_s - T_{evap})} \quad (5)$$

where A_s is the impingement surface area, T_{evap} is the evaporating temperature and \dot{Q}_c^* is the corrected cooling capacity, i.e., the fraction of the input heat load, \dot{Q}_c , that actually reaches the impingement surface of the copper block. The procedure to determine \dot{Q}_c^* was outlined in detail in Ref. [?], with the relative difference between \dot{Q}_c^* and thermal load being of the order of 5% for all tests.

The temperature of the surface of the copper block, T_s , was determined through a linear extrapolation of Fourier's law considering 1-D heat conduction in the axial direction,

$$T_s = \bar{T}_{RTD} - \frac{L_s \dot{Q}_c^*}{k_s A_s} \quad (6)$$

where L_s is the distance between the copper block surface and the plane of the RTDs and k_s is the thermal conductivity of copper evaluated at \bar{T}_{RTD} , which is the arithmetic mean of the five RTDs used to measure the copper block temperature.

In the present analysis, the coefficient of performance, COP , was defined so as to account for the energy consumption strictly necessary to remove the heat load imposed on the jet cooler. Thus:

$$COP = \frac{\dot{Q}_c}{\dot{W}} \quad (7)$$

where $\dot{W} = \dot{W}_{comp} + \dot{W}_{fan}$ is the sum of the power consumptions of the compressor and fan (recommended by the compressor manufacturer to cool the compressor shell).

1.4. Energy balances and experimental uncertainties

As discussed in Ref. [?], energy balances were executed on the experimental apparatus for each experimental test to verify the consistency of the measurements. The first-law ([energy](#) balance) residue, δ_{1st} , is defined as the difference between the heat transfer rates out of and into the refrigeration system,

$$\delta_{eb} = \frac{|\dot{Q}_{cond} - (\dot{Q}_c + \dot{Q}_{sh} + \dot{W}_{ind})|}{\dot{Q}_c + \dot{Q}_{sh} + \dot{W}_{ind}} \times 100\% \quad (8)$$

Additionally, a compressor calorimeter has been specially designed and constructed to provide a direct measure of the rate of heat dissipation by the compressor through its shell. A full description of the calorimeter is given in Refs. [? ?].

For the tests reported in this paper, the average value of δ_{eb} was 0.9%, which confirms that the [energy](#) balance was fully satisfied and that the experimental facility was properly insulated and the energy transfer rates were measured accurately. The compressor calorimeter energy balance was also satisfied (despite the somewhat larger average residue of 9.2%), indicating that the energy transfer rates to and from the oil-free compressor were also measured accurately.

Table 1 presents the expanded uncertainties for the calculated parameters, according to the procedure of Ref. [?]. As these uncertainties vary according to each experimental run, only the maximum values are reported [?].

Table 1: Expanded uncertainties (maximum values) of the calculated parameters.

Calculated parameters	Expanded uncertainty
\dot{Q}_c [W]	1.77
\dot{W}_{comp} [W]	4.53
COP [-]	0.49
x_6 [-]	0.013
h_s [W m ⁻² K ⁻¹]	433.0
T_s [°C]	0.10
T_{cond} [°C]	0.10
T_{evap} [°C]	0.26
ΔT_{sc} [°C]	0.18

2. Results

2.1. Effect of the Orifice-to-Heater Distance (Jet Length)

In this section, the results were generated for a hot source temperature fixed at $T_7 = 15^\circ\text{C}$. For convenience, the jet cooler parameters are evaluated first and the system performance is analyzed next. In order to provide a meaningful basis for comparing the results obtained with the two jet lengths, H , the same refrigerant mass flow rate was enforced in the tests with a piston stroke of 50% and cooling capacity of 25 W. This was achieved by adjusting the refrigerant mass (charge) in the system.

Considering similar operating conditions (α and \dot{Q}_c), Fig. 5 (a) suggests that T_s is insensitive to the change in the jet length. Nevertheless, it is important to observe in the same figure that, for the intermediate and full stroke conditions, the reduction of H shifted the point of dryout (CHF)

to lower cooling capacities. This point corresponds to the highest cooling capacity for each curve and, as mentioned above, is associated with a drastic increase of the heater surface temperature, resulting in the interruption of the experiment. As can be seen, the reduction of the CHF was very dramatic, with a maximum decrease of approximately 85 W for the 100% piston stroke in comparison with the tests with a larger H . A clear reduction of the heat transfer coefficient was also observed when H was shortened from 28.84 to 9.75 mm, as seen in Fig. 5 (b).

The behavior of the evaporating temperature is shown in Fig. 6. While the results for the two values of H are very similar for $\alpha = 50\%$, the evaporating temperature for smaller jet lengths is reduced as the cooling capacity increases for $\alpha = 75\%$ and 100% . Thus, the net effect of the results shown in Figs. 5 and 6 is an increase of the wall superheat, $(T_s - T_{evap})$, as H is reduced from 28.84 mm to 9.75 mm.

For a fixed thermal load, it became clear that the increase in wall superheat was caused by a reduction of the thermal conductance associated with the jet impingement configuration. Jet splattering and droplet breakup were the major factors contributing to the reduction of the heat transfer coefficient shown in Fig. 5 (b). Splattering was visually observed to increase considerably when the jet length was reduced from 28.84 to 9.75 mm. Since the pressure ratio and the refrigerant mass flow rate were quite similar for the two values of H , the jet impact velocity is expected to be greater for the shorter jet length, which is likely to promote a more vigorous atomization of the liquid into droplets ejected from the heater surface. By having a lower flow rate of liquid as a continuous film on the surface, both the heat

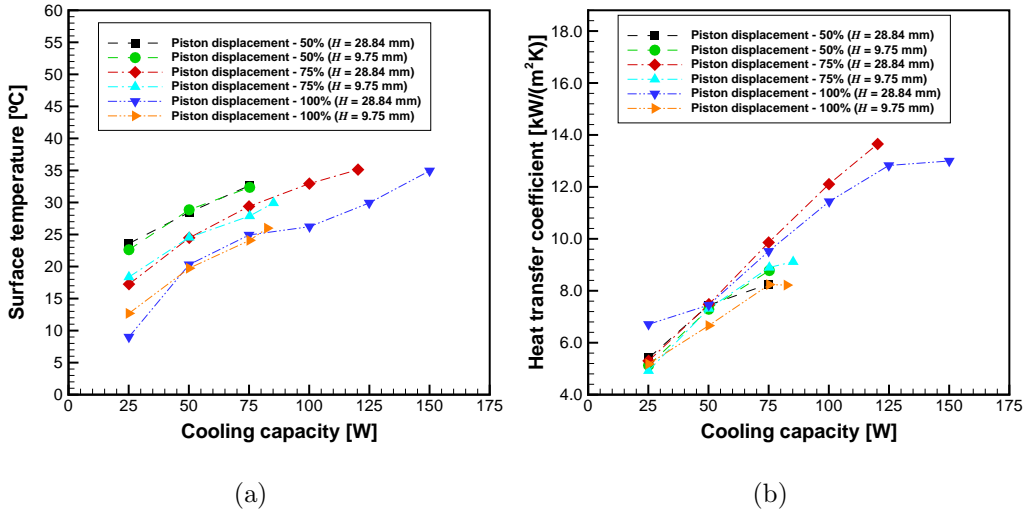


Figure 5: Jet cooler heat transfer parameters as a function of the applied heat load (cooling capacity) for different piston strokes and jet lengths. (a) Surface temperature. (b) Heat transfer coefficient. Formato unidades HTC IJR na fig b

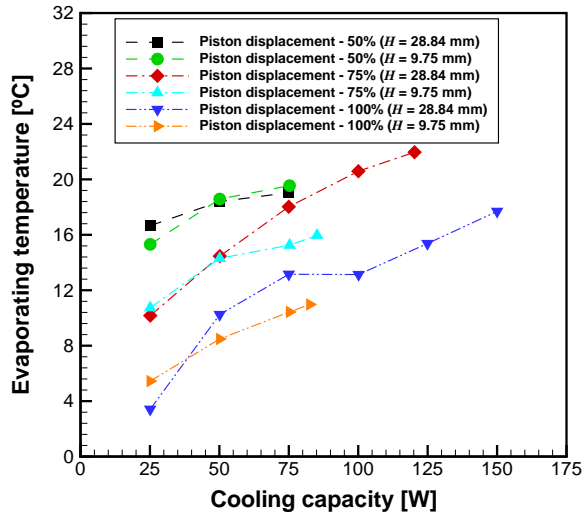


Figure 6: Evaporating temperature as a function of the applied heat load (cooling capacity) for different piston strokes and jet lengths.

transfer coefficient and the CHF associated with the smaller H are reduced in comparison with the larger jet length.

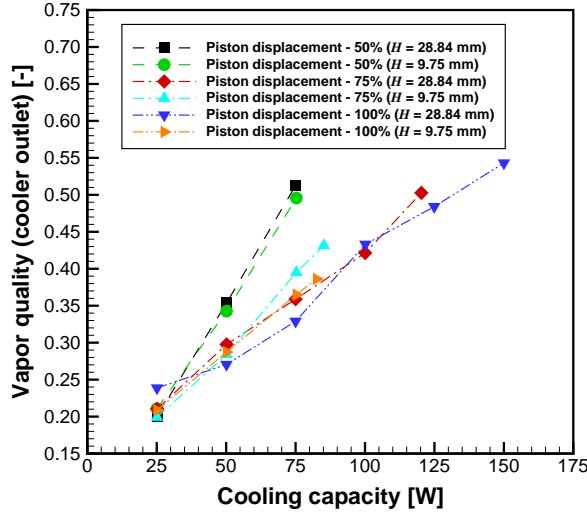


Figure 7: Outlet vapor quality as a function of the applied heat load (cooling capacity) for different piston strokes and jet lengths.

From an operation standpoint, the reduction of the CHF appears to be more important than the deterioration of the heat transfer coefficient. The effect of this reduction can also be perceived by looking at the behavior of the outlet vapor quality presented in Fig. 7. While the highest vapor qualities for the smaller jet length (considering piston strokes of 75% and 100%) are approximately 43% and 39%, the corresponding values for the longer jet are 50% and 54%, respectively, which means that the latent heat (enthalpy) of vaporization of the refrigerant is used much more effectively for a jet length of 28.84 mm.

Figure 8 illustrates the effect of the jet length on the thermodynamic cycle for $\alpha = 100\%$ and $\dot{Q}_c = 75$ W. A clear shift towards lower condensing

and evaporating pressures is observed due to the reduction of the pressure lift.

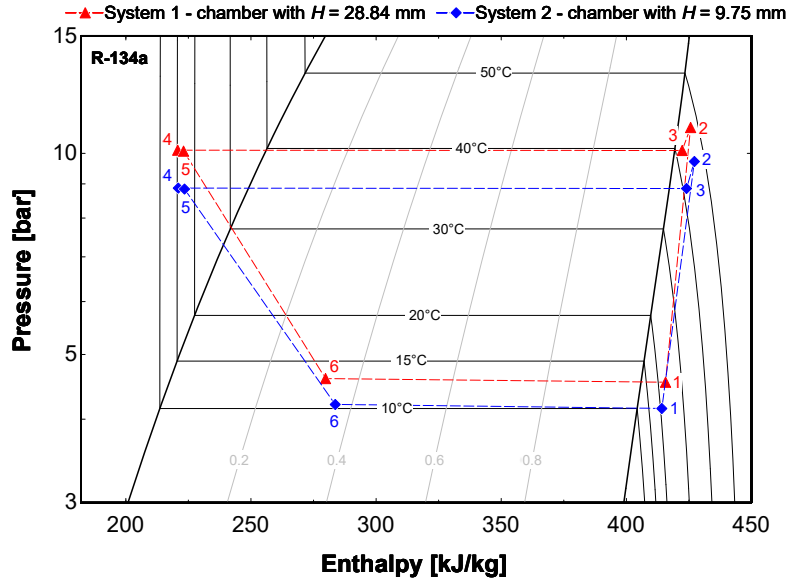


Figure 8: *P-h* diagram: comparison between different jet lengths for the same piston stroke (100%) and cooling capacity (75 W). The numbers refer to the diagram in Fig. ??.
unidade formato IJR eixo x

Nevertheless, the effect of the above-mentioned pressure shift on the compressor power consumption is rather small, as seen in Fig. 9 (a). Therefore, the *COP* is mildly affected, i.e., there is only a slight increase for piston strokes of 75% and 100%, as depicted in Fig. 9 (b).

2.2. Effect of the Hot Reservoir (Ambient) Temperature

This section is dedicated to the analysis of the effect of the hot end (secondary fluid) temperature, T_7 . The experimental tests were run only at 100% compressor stroke, for it has been shown [? ?] that it is more

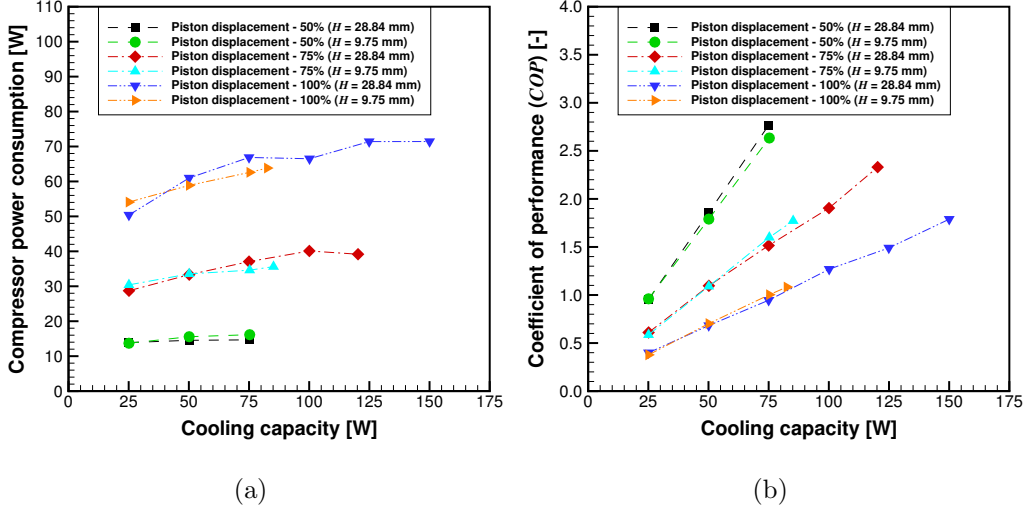


Figure 9: (a) Compressor power consumption and (b) *COP* as a function of the applied heat load (cooling capacity) for different piston strokes and jet lengths.

(thermodynamically) advantageous to operate the active cooling system at such conditions.

Operating the system at a higher hot end temperature (HET) increases the condensing temperature compared to the cases for which $T_7 = 15^\circ\text{C}$, as shown in Fig. 10 (a). In addition, a higher hot end temperature necessarily increases the refrigerant temperature at the condenser outlet, T_4 . As the rise in T_7 is significantly higher than the increase in T_4 for both hot end temperatures, the sub-cooling degree, defined as $\Delta T_{sc} = T_{cond} - T_4$, decreases as exhibited in Fig. 10 (b). Therefore, the coolant reaches the jet heat sink at a higher temperature.

The temperature after expansion, i.e., the evaporating temperature, is also higher compared to the test conducted with the lower ambient temperature, for the same cooling capacity. The behavior of T_{evap} is presented in

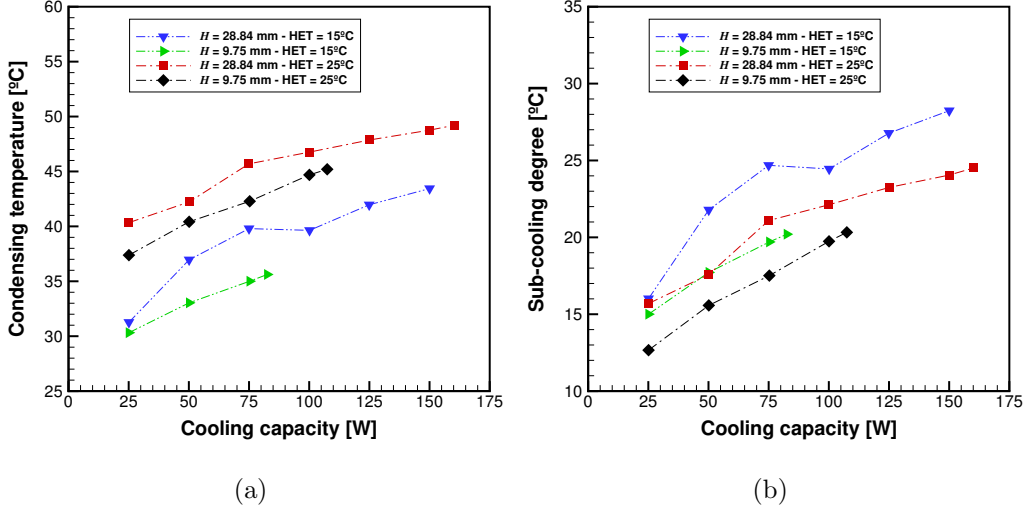


Figure 10: (a) Condensing temperature and (b) sub-cooling degree as a function of the applied heat load (cooling capacity) for different jet lengths and hot end temperatures (HET).

Fig. 11 (a). The increase of the saturation temperatures generates a higher pressure lift, which is confirmed by the noticeable increase of the electrical power consumption of the compressor, as depicted in Fig. 11 (b).

For the same jet length, Fig. 12 (a) shows that the surface temperature changes little with the ambient temperature. As the evaporating temperature is observed to increase with an increase in T_7 , the wall superheat becomes lower, which is, essentially, a manifestation of the higher heat transfer coefficient shown in Fig. 12 (b). The increase in \bar{h}_s is a consequence of the mass flow rate increase with the cooling capacity as the refrigerant density at the compressor inlet is raised due to the higher evaporating pressures [?].

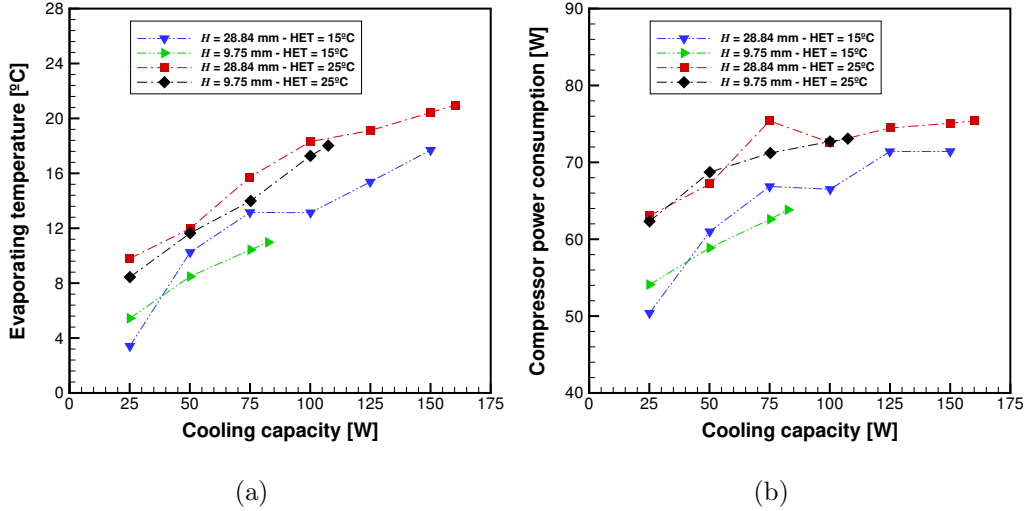


Figure 11: (a) Evaporating temperature and (b) compressor power consumption as a function of the applied heat load (cooling capacity) for different jet lengths and hot end temperatures (HET).

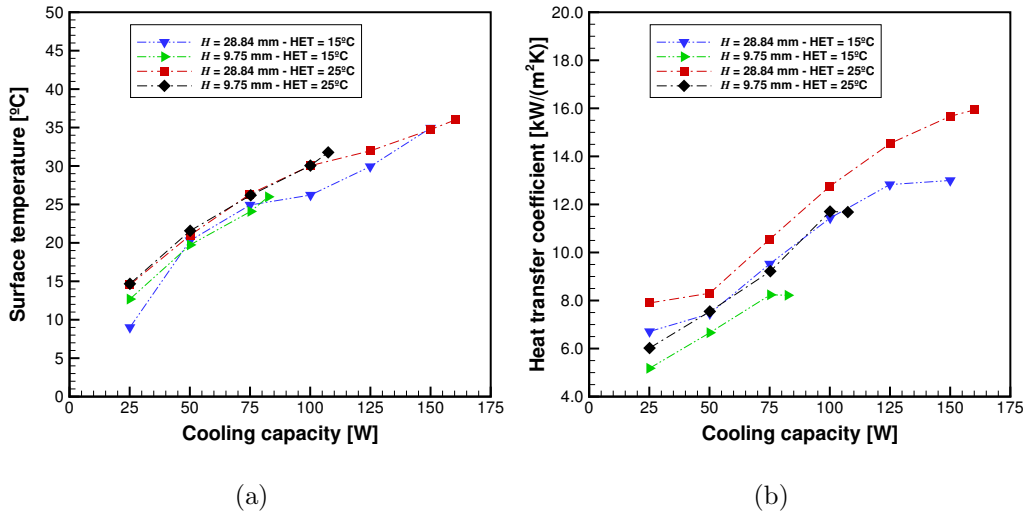


Figure 12: (a) Surface temperature and (b) heat transfer coefficient as a function of the applied heat load (cooling capacity) for different jet lengths and hot end temperatures (HET). unidades HTC IJR format eixo y

3. Conclusions

A novel two-phase jet heat sink that integrates the evaporator and the expansion device into a single cooling unit has been presented and evaluated. The new jet cooler was combined with a compact oil-free linear motor R-134a compressor to demonstrate the applicability of the system in the removal of high heat loads. Experiments have been carried out with a single-orifice configuration of the jet heat sink ([300- \$\mu\text{m}\$ diameter](#)). The main conclusions arising from this work are as follows:

1. Reducing the jet length from 28.84 mm to 9.75 mm increased jet splattering and droplet breakup. This reduced the heat transfer coefficient and, more significantly, the critical heat flux. However, the impact on the heater surface temperature, compressor power consumption and coefficient of performance was minimal;
2. For a fixed jet length, increasing the hot reservoir temperature from 15°C to 25°C caused an increase in both the evaporating and condensing temperatures. The net effect of this change was an increase of the heat transfer coefficient resulting from the higher mass flow rate. However, as expected, an increase in the compressor power was observed.

Acknowledgements

This work was made possible through the financial investment from the EMBRAPII Program (POLO/UFSC EMBRAPII Unit - Emerging Technologies in Cooling and Thermophysics). In addition, financial support from Embraco and from CNPq (Grant No. 573581/2008-8 - National Institute

of Science and Technology in Cooling and Thermophysics) is duly acknowledged.

References